Article
Vol. 25, No. 4, p. 547–559, August 2021
https://doi.org/10.1007/s12303-021-0011-9
pISSN 1226-4806 eISSN 1598-7477
Geosciences Journal GJ

Assessing the effects of external factors on sediment erosion and accumulation in an estuarine environment based on images from unmanned aerial vehicles: Namdae-cheon, South Korea

Seulki Lee[1], Jinah Eom[1], Mutiara Syifa[1], Sung-Jae Park[1], Yu-Chul Park[2], and Chang-Wook Lee[1]*

[1]Division of Science Education, Kangwon National University, 1 Kangwondaehakgil, Chuncheon-si, Gangwon-do 24341, Republic of Korea
[2]Department of Geophysics, Kangwon National University, 1 Kangwondaehakgil, Chuncheon-si, Gangwon-do 24341, Republic of Korea

ABSTRACT: Estuaries include dynamic patterns of channels, which serve as valuable habitat. The Namdae-cheon estuary is a closed estuary due to the natural dunes surrounding it, making monitoring particularly important. The use of unmanned aerial vehicles (UAVs) has considerable promise for monitoring dynamic areas such as the Namdae-cheon estuary. They are easy to use and can be implemented to obtain a high-resolution digital surface model (DSM) and georeferenced images. We monitored the Namdae-cheon estuary two times in a 1-month period (on November 20 and December 18, 2018). The estuary experienced significant morphological changes during the study period. The height of the sandbar sediment was reduced by about 30 cm, as revealed by DSM of difference (DoD) analyses. Sediment samples were also analyzed and used to explain the dominant factors influencing sedimentation in the estuary. By combining DSM data from UAV photos with sediment sample data, it was possible to explain the causal factors of morphological changes and infer the direction of sediment movement in the study area. Tidal factors, wind speed, and rainfall all influenced morphological changes and sedimentation. Overall, UAV photos and the resulting DSM, orthophotographs, and DoD provide abundant information for studies monitoring morphological changes.

Key words: Namdae-cheon estuary, UAV, DSM, grain fineness number analysis, morphological changes

Manuscript received May 25, 2021; Manuscript accepted June 8, 2021

1. INTRODUCTION

An estuary is an area that has river water flow at the landward boundary and an open flow to the sea. In general, estuaries are distinct based on the relative influences of rivers, waves, tides, sediment supplies, sediment types, vegetation, geology, and time (Savenije, 2012). The estuary represents a specific environment, where freshwater from a river is mixed with salty water from a sea, that has rich biodiversity and ecological services. The complexity of estuarine systems arises from their variety of interconnected areas, such as main a channel, lateral mudflat, and ebb-tidal delta bank areas. Estuaries often include temporary and spatially variable processes of sediment dynamics and morphodynamics (Dyer, 1995; Green et al., 1997; Friedrichs et al., 1998). The intertidal mudflat is a significant feature in complex estuarine ecosystems. The lateral edges, including a mixture of sediments (clay, silt, sand) from the main channel, which are sequentially flooded and exposed by tidal variation and river discharge, play an essential role in the dynamics of estuarine sediments as a source or sink of transient sediments (Deloffre et al., 2005, 2007). In-depth analyses of surface sediment features are very important for monitoring ecosystem health, evaluating sediment dynamics, and planning coastal engineering actions.

Hydrological factors, which include river flow and suspended solid inputs from land, meteorological factors, including wind and waves, and hydrodynamic forces, such as tides, control the dynamics of estuary sediments, and hence mudflat morphodynamics, at different time scales. Morphological changes related to erosion or deposition events lead to changes in the height of the mud layer, or tidal channel development and migration. Fluvial

*Corresponding author:
Chang-Wook Lee
Division of Science Education, Kangwon National University, 1 Kangwondaehakgil, Chuncheon-si, Gangwon-do 24341, Republic of Korea
Tel.: +82-33-250-6731, E-mail: cwlee@kangwon.ac.kr

morphodynamics is the outcome of multifarious interactions between water flow, sediment transport, and riparian vegetation (Marion et al., 2014; Gurnell et al., 2016; Nones and Di Silvio, 2016). The results of these complex interactions have a problematic impact on the forecasting of channel cross-section evolution, the displacement of partially emerged bars, and the quantification of bank erosion, which typically require detailed numerical modeling. The calibration of such models requires in-field data, which can be collected from topographic surveys. Therefore, improved monitoring techniques that can obtain high-resolution information remotely are needed to continuously characterize the fluvial environment irrespective of the water stage and atmospheric conditions. Several techniques for monitoring coastal and river morphodynamics and the displacement of waterlines have been used by the scientific community. These methods have been based on the use of kinematic differential global positioning systems (DGPS), the post-processing of historical maps (Scorpio et al., 2018), data acquired remotely by satellites (Domeneghetti, 2016; Payne et al., 2018), airplanes (Moretto et al., 2014; Spiekermann et al., 2017), and more recently, unmanned aerial vehicles (UAVs) (Langhammer et al., 2017), and the analysis of video camera images (Archetti et al., 2016).

UAVs have become an alluring method in many fields of research for obtaining the latest information from target areas due to their high mobility, excellent resolution, and minimal costs (Remondino et al., 2011; Haubeck and Prinz, 2013; Siebert and Teizer, 2014). Currently, UAVs with autonomous navigation functions have achieved a level of practical consistency and have become a beneficial platform for attaining spatial data. UAV photogrammetry can generate morphologic data in a short time and facilitate the production of high-resolution digital models of complex environments with the obligatory accuracy. These devices have broad prospective applications, such as for environmental monitoring and management, agriculture, mining, surveying, and conservation.

Several studies have assessed the photogrammetric potential of UAVs (Gülch, 2011; Haala et al., 2011; Küng et al., 2011; Vallet et al., 2011; Rosnell and Honkavaara, 2012; Barry and Coakley, 2013). Small UAVs are mostly used in small areas and can obtain high resolution by maneuvering into close proximity of the subject. Ground control points (GCPs) help to position the acquired map more accurately in relation to the real world. A UAV allows a user to supervise the results and repeat the mapping process if the outcome is considered unsatisfactory. Remotely sensed imagery and geospatial image processing using unmanned aerial systems (UASs) can support rapid and ongoing observation tools that may allow better monitoring of dynamic areas such as the Namdae-cheon estuary in Korea. This study describes a UAS-based remote-sensing method intended to increase the effectiveness of existing practices for discovering morphological changes in an estuary.

2. MATERIALS AND METHOD

The Namdae-cheon estuary is located in Yangyang, Gangwon Province, South Korea (Fig. 1a). The estuary originates from Doolubong in Ganggye-myeon, Gangneung, and joins with streams from the valleys of Mt. Seorak, Mt. Jokbong, Ngokbuksan, and Huangbashan in the Taebaek Mountains (Byeon et al., 1996). The population of Namdae-cheon is small, and the area has little industrial activity. These factors, combined with the geographical isolation of the mountainous regions, have allowed the environment to remain relatively pure. The average water depth is around 1 m, resulting in extreme temperature differences between winter and summer. In addition, floods and high waves cause cyclic invasions that connect lagoons with the sea. These invasions allow chub mackerel, flatfish, black sea bream, gizzard shad, and other species to live near streams instead of the more typical carp and Asian sea fish. Species such as cold-water fish, aquatic fish, and Japanese reptiles are becoming more abundant. This contrasts with the dominance of salmon, which are particularly common in domestic rivers (Yoon et al., 1999). The Namdae-cheon estuary is a closed estuary because of the natural sand shoals around it. Hence, water does not flow smoothly into the ocean and becomes stagnant. In addition, the penetration of some seawater through the opening and the closing of separate channels causes density stratification that depends on salinity. Therefore, organic flow from the upstream area or from the adjacent soil can cause environmental degradation in the estuary, such as eutrophication. Long residence times in the downstream area cause organic matter to stagnate and nutrition to accumulate, resulting in a decrease in water quality (Yoon et al., 1999).

UAV photographs of the Namdae-cheon estuary were acquired through the nadir (vertical) viewing direction on two dates, November 20 and December 18, 2018, using a DJI Phantom Pro 4 drone, and planned using the map pilot app Pix4Dcapture. GCPs were placed roughly at the center of each sandbar range, and the layout was considered sufficient to adequately constrain the drone range control. The average flying height, directed by autopilot, was 60 m above ground level (AGL). Each 12-megapixel photograph covered about 431,392 m^2 on the ground, resulting in 2 cm resolution imagery. On November 20, 2018, 604 UAV photographs were obtained; on December 18, 2011, 547 photographs were acquired (Figs. 1b and c). The GPS data were provided from the drone observation as shown in drone imagery by red points in Figure 1b and green points in Figure 1c. Camera alignment was adjusted with bundle adjustments. Common

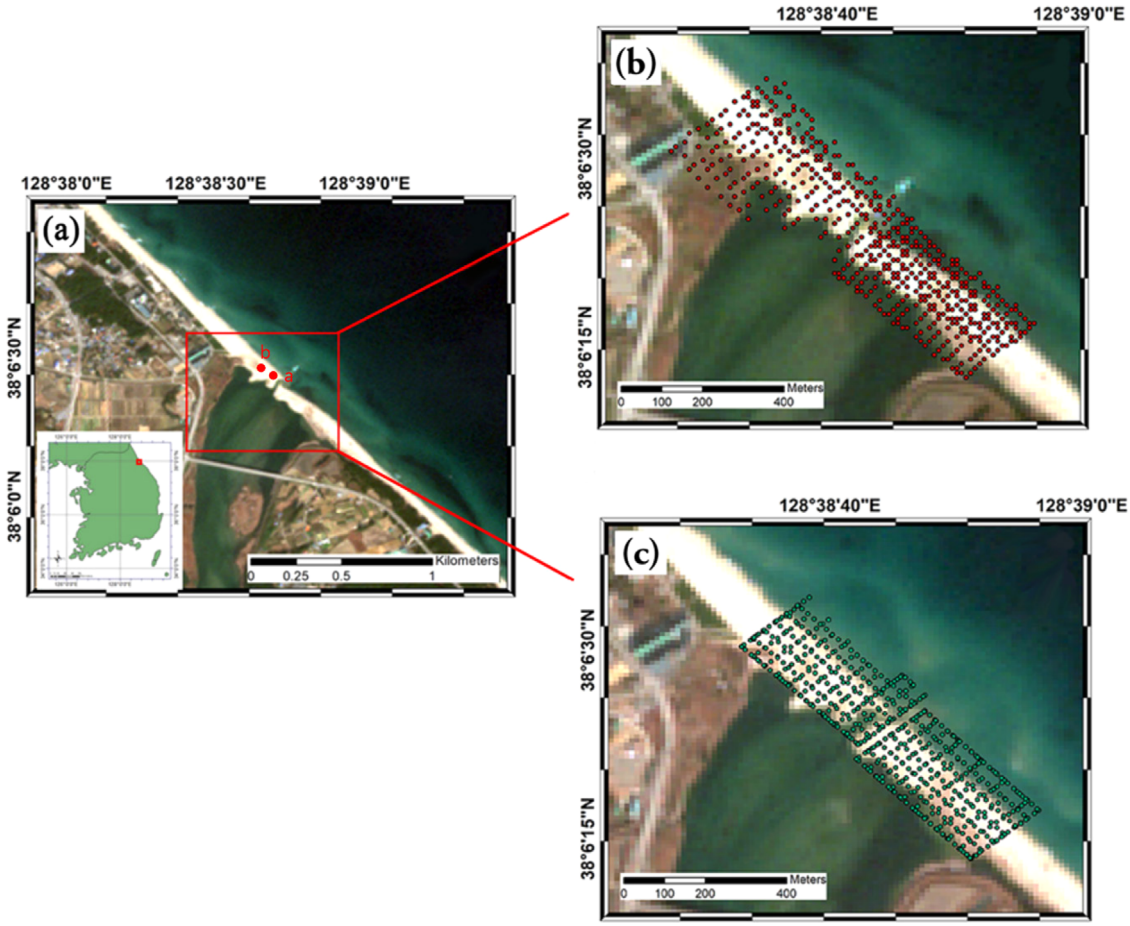

Fig. 1. Location of the study area: (a) map of Korea and a Sentinel image. The red points represent the location of field measurements using hand GPS devices. Zoom of a study area from Sentinel image shown the overlapping images and computed camera positions for the two surveys (b) November 20, 2018, (c) December 18, 2018. The red and green points represent the number of GPS data acquired by the drone observation on different dates.

bond points were perceived and matched on overlapping photos so that external camera factors (position and orientation) for each image and accurate camera calibration parameters could be calculated (Woodget et al., 2015; Jaud et al., 2016).

The procedure for deriving orthophotographs and the digital surface model (DSM) was based on the structure from motion (SfM) workflow for multiview stereophotogrammetry (MVS). An orthophotograph is defined as an aerial photograph mosaic that is geometrically corrected for lens distortion and ground relief effects. Orthophotographs have an equal scale throughout and can be utilized as maps (Javernick et al., 2014). The SfM method begins by obtaining photographs from the object of interest, within sufficient overlap (e.g., 80–90%), which can be taken from multiple points and angles (Lucieer et al., 2014). GCP and the incorporation of camera GPS locations support 3D model georeferencing in a real-world coordinate scheme. Finally, the model can be transferred to a grid-based DSM, and orthophoto mosaics (orthomosaics) can be produced from the projected and blended photographs (Fig. 2).

Basically, a digital elevation model (DEM) is a grid-based representation of topography, which is built by topographic point interpolation. However, a DSM shows the elevations of the ground and all features on it, such as buildings and vegetation. On the other hand, a digital terrain model (DTM) is a representation of the bare ground (Maune, 2001). This study focused on a DSM, straightforwardly determined by PhotoScan because DSMs are easier to process than DTMs and DEMs. However, the DSM and DEM in the main part of the study area were identical. Thus, the terms DSM and DEM are used interchangeably in the following explanations. In addition, we obtained elevation data in the field using field measurements and hand GPS devices (Table 1). Each data-collection point was marked using a 1-m pipe, and a portion of the pipe was buried to a depth of 50 cm to calculate the sedimentation rate during the study period. Field measurements were carried out on November 20 and December 18, 2018, and then the results were compared to determine whether accretion or erosion of sediment had occurred. Two points were used to measure elevation.

https://doi.org/10.1007/s12303-021-0011-9

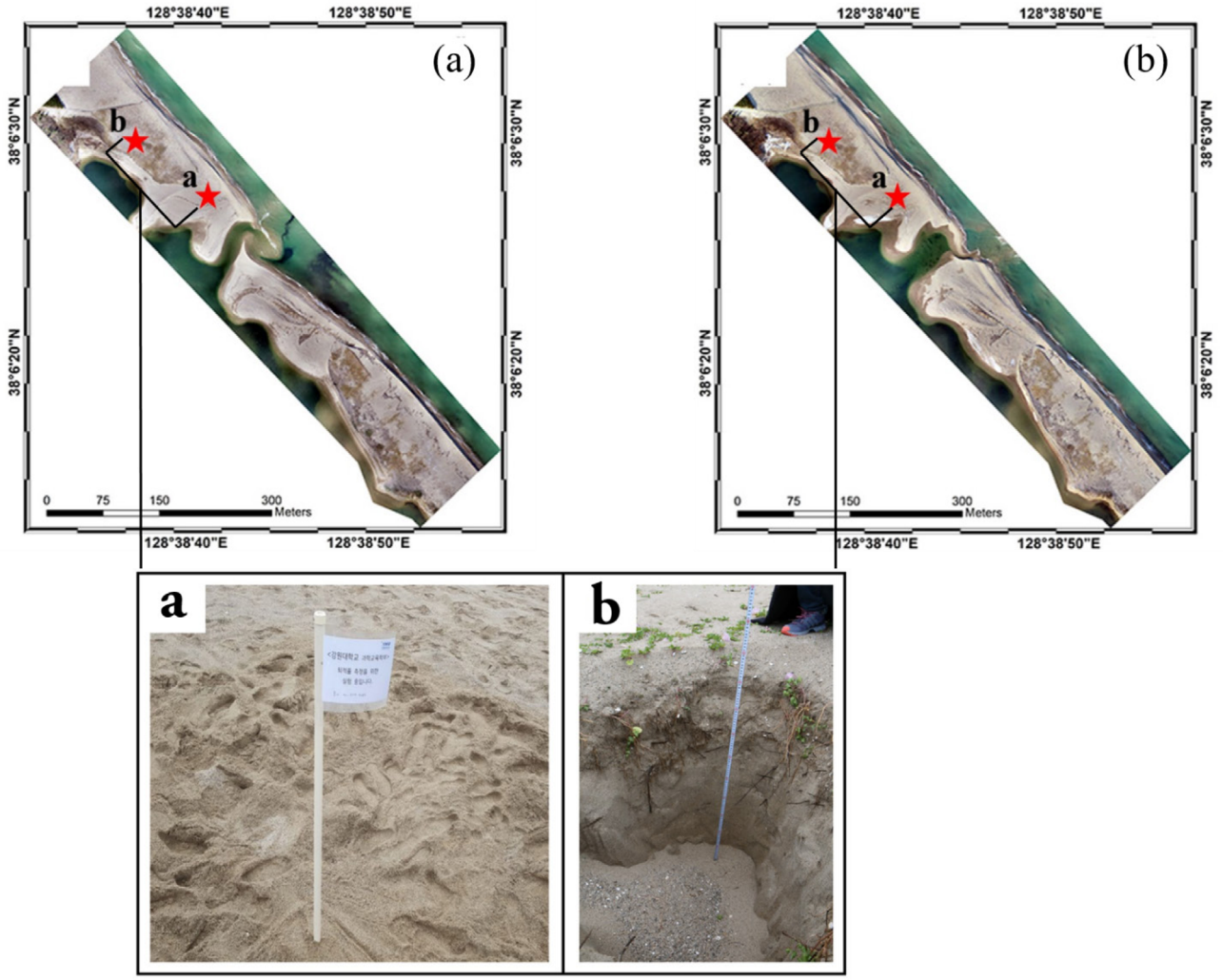

Fig. 2. Orthophotographs of the study area and GPS points: (a) November 20, 2018, (b) December 18, 2018, which shows the photographs of sediment sampling from location a where the sediment sampling point is shown and location b which shows depth of sediment sampling.

Table 1. Location of GPS data and field measurements with comparison of difference elevation from DSM data and field data

Point	Latitude	Longitude	Height on November 20th, 2018 (cm)	Height on December 18th, 2018 (cm)	Difference	
					From DSM (cm)	From Field (cm)
a	38°6′29.716″N	128°38′37.095″E	59	60	−4.2	−1
b	38°6′27.322″N	128°38′41.207″E	78	93	−12.7	−15

Sediment samples from the estuary were collected by Lee et al. (2018) on March 31, 2017, at 24 sampling sites around the sandbar (Table 2). Among these, 13 sites (points P1–P13) were at the northwest sandbar and 11 sites (P14–P24) were at the southeast sandbar. The sand was dug to a depth of about 100 cm, and sediments were sampled at depths of 20, 40, 60, 80, and 100 cm (Fig. 2). The sampling locations were plotted using handheld GPS units and a GPS drone (Fig. 3). The sediment samples were used for numerical analyses of grain fineness and moisture content analyses. Both were expected to influence the sedimentation dynamics in the study area.

Grain fineness values (i.e., particle diameters) are used in sediment studies. However, a standard reference scale is needed to distinguish particles of different sizes because the sizes of sediment particles vary greatly. For example, Udden (1898) set the reference value at 1 mm. Particle size boundaries greater than the reference value are twice the size of the subjacent value in the scale, and particle size boundaries smaller than the reference value are half the size of the superjacent value in the scale. A 1 mm size difference is important for particles the size of sand, but it is less important for gravel and larger clasts because it can be considered within the range of measurement

Table 2. Locations of sediment sampling sites

Sites	Latitude	Longitude	Sites	Latitude	Longitude
P1	38°6′31.44″	128°38′36.42″	P13	38°6′24.86″	128°38′40.81″
P2	38°6′30.83″	128°38′35.41″	P14	38°6′23.22″	128°38′45.27″
P3	38°6′29.92″	128°38′38.76″	P15	38°6′22.63″	128°38′44.48″
P4	38°6′29.51″	128°38′38.26″	P16	38°6′22.16″	128°38′43.76″
P5	38°6′28.97″	128°38′37.54″	P17	38°6′21.34″	128°38′48.28″
P6	38°6′28.02″	128°38′41.09″	P18	38°6′21.16″	128°38′47.68″
P7	38°6′27.67″	128°38′40.52″	P19	38°6′20.54″	128°38′47.11″
P8	38°6′27.19″	128°38′40.04″	P20	38°6′20.01″	128°38′46.57″
P9	38°6′26.62″	128°38′39.32″	P21	38°6′19.40″	128°38′49.95″
P10	38°6′26.63″	128°38′42.79″	P22	38°6′18.61″	128°38′49.22″
P11	38°6′26.29″	128°38′42.20″	P23	38°6′17.73″	128°38′51.81″
P12	38°6′25.64″	128°38′41.45″	P24	38°6′16.90″	128°38′50.74″

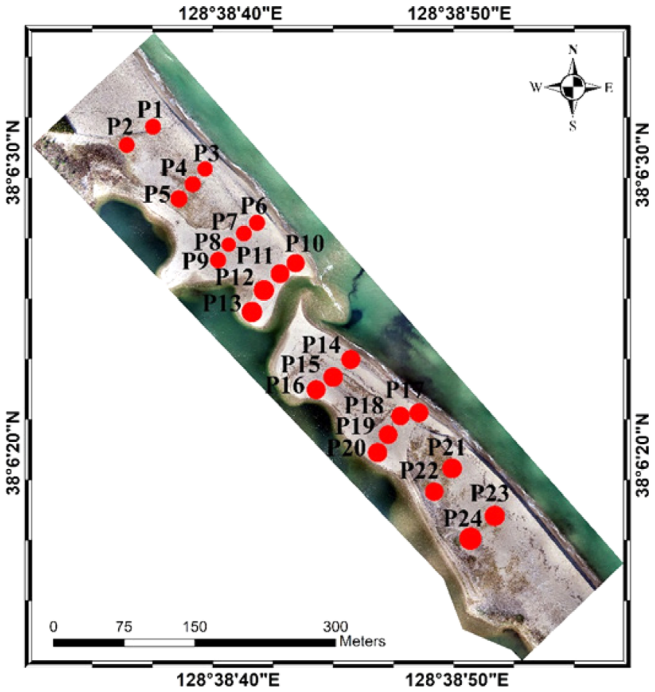

Fig. 3. Locations of sediment sampling from orthophotograph.

error. To overcome this problem, Krumbein (1934) noted that it is more convenient to express millimeter-based particle size on a logarithmic scale. Therefore, the standard particle sizes widely used by Udden (1898) were defined as phi (ϕ) values. Wentworth (1922) also developed a scheme used as a standard classification scale. Table 3 shows particle sizes in mm and ϕ and also shows the terms for the particle size categories corresponding to each section (Lee et al., 2016).

In this study, the particle sizes of dried sand samples were analyzed by sieve analyses using standard sieves. The sizes of the particles on the phi (ϕ) scale were determined, as shown by Equation (1):

$$\phi = -\log^2\left(\frac{d}{d_0}\right), \quad (1)$$

where d represents the diameter of the particle in mm and d_0 is a reference diameter of 1 mm. Classification of sediment particle size by the Udden-Wentworth Scale (Wentworth, 1922) was used.

Particle diameter can be determined using a screen or by measuring it directly from thin sections. The sediment particle size distributions were analyzed using numerical values to determine the cumulative frequency curve, mean values, modes, median values, classification, slope, and kurtosis. These statistics can be calculated using the moment method by changing the particle size data into the ϕ standard. Graphs based on data using phi standards are more commonly used than moment calculations because the largest or smallest particle size is uncertain. In this study, particle size analyses were carried out as shown in Equations (2)–(5) by applying the method proposed by Folk and Ward (1957). For example, ϕ16, ϕ50, and ϕ84 represent the cumulative weight percentages of 16%, 50%, and 84%, respectively.

$$\text{Mean} = \frac{(\phi 16 + \phi 50 + \phi 84)}{3}, \quad (2)$$

$$\text{Sorting} = \frac{(\phi 84 + \phi 16)}{4} + \frac{(\phi 95 - \phi 5)}{6.6}, \quad (3)$$

$$\text{Skewness} = \frac{\phi 84 + \phi 16 - 2\phi 50}{2(\phi 84 - \phi 16)} + \frac{\phi 95 + \phi 5 - 2\phi 50}{2(\phi 95 - \phi 5)}, \quad (4)$$

$$\text{Kurtosis} = \frac{\phi 95 - \phi 5}{2.44(\phi 75 - \phi 25)}. \quad (5)$$

3. RESULTS

3.1. Digital Surface Model

The lowest elevation point in each model was used to decide

https://doi.org/10.1007/s12303-021-0011-9

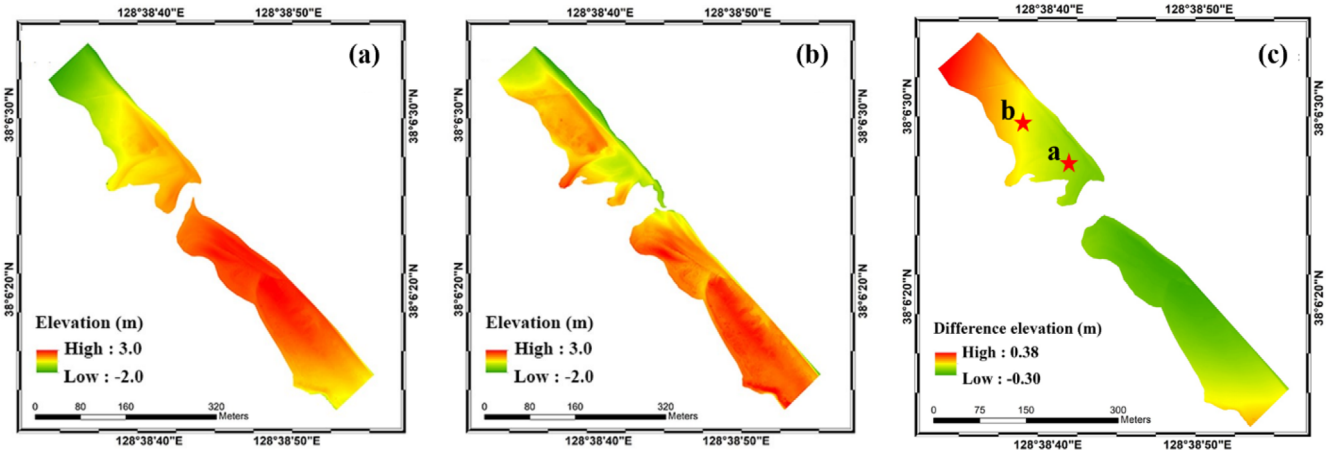

Fig. 4. DEM resulting from the survey of (a) UAV imagery acquired on November 20, 2018, (b) UAV imagery acquired on December 18, 2018, and (c) DSM of difference in the study area between November 20, 2018, and December 18, 2018.

the terrain surface, because the lowest elevation point is most likely to show the ground within vegetated areas (Javernick et al., 2014). In all analyses, the SfM photogrammetry used to compute the orthophotograph and the DSM provided a surface representation of the study area (Figs. 4a and b). Based on the DSM data, the sandbar surface height ranged from –2 to 3 m above sea level. The DSM data also showed that the study area experienced significant changes in the period from November 20 to December 18, 2018, including changes in sandbar elevation as well as morphology, particularly in the river estuary section between the northwest and southeast sandbars. Thus, it can be stated that the research area is a dynamic area with frequent morphological changes.

Recurring high-resolution DSM data are useful for assessing and monitoring erosion and deposition, calculating volumetric changes over a specific time, and assessing sediment budgets (Brasington et al., 2003; Wheaton et al., 2010). After assembly, the DSM and orthophotograph data were transferred into a reference coordinates system. The DSM data were differentiated into two diachronic DSMs to compute a DSM of difference (DoD), i.e., a change grid in elevation within two acquirement dates. The DSMs were subtracted using ESRI ArcGIS® software. By subtracting the previous DSM from the more recent one, the DoD generated shows erosion as a negative value and accretion as a positive value. The DSM subtraction of November 20, 2018, from December 18, 2018, provided a general spatial representation of the morphological evolution, which can be seen in Figure 4c. The tidal creek located in the middle part of the area was highly mobile because of the drastic sediment changes. Based on the DoD image, the height of the sandbar decreased by about 0.3 m in almost all parts of the sandbar, except in the northern part, where it increased by about 0.3 m. Overall, these results indicate that the sediment in the sandbar of the study area was lowered or eroded. Study of typical sedimentary structures in the intertidal zone of the sandbar is possible because UAV photogrammetry is a multi-scale method. For instance, the tidal-creek morphodynamics located in the middle of the survey area can be depicted with excellent resolution and accuracy, revealing good geomorphological variation (in centimeter). Rapid migration of the tidal mouth (connected to the main channel) was attained, as was the morphological progression of the sandbar.

GPS data were used to monitor the coordinates of the sedimentation on the sandbar. Two coordinate observation points on the sandbar were taken. The results of the calculation of the difference in sediment height on the sandbar from the DSM and from the field measurement are shown in Table 1. The DSM data and the field data showed that the sandbar sediment was eroded. The field measurement data indicated that observation point A had sediment erosion of 1 cm and that observation point B had erosion of 15 cm. According to the DSM data, observation point A had erosion of 4.2 cm and observation point B had erosion of 12.7 cm. The two measurement results differ slightly, but are in general agreement.

3.2. Grain Fineness and Moisture Content Analyses

The sedimentary depositional characteristics in the study area were determined by analyzing data from 24 sample sites, 13 on the west side of the estuary and 11 on the east side. At each sample site, five samples were collected (at depths of 20, 40, 60, 80, and 100 cm) and analyzed for grain fineness, classification skewness, and kurtosis.

Table 3 and Figure 5 show the results of particle size analyses. The average particle size at each sampling location was calculated and classified according to the Udden-Wentworth scale. The average size ranged from 0.67 to 1.28 mm, indicating that the

Table 3. Analysis of parameter by location (Lee et al., 2018)

Site	F (mm)	C (φ)	S	K	Site	F (mm)	C (φ)	S	K
P1	1.07	0.35	2	0	P13	0.92	0.29	1.75	0
P2	0.87	0.5	0.2	0.41	P14	0.8	0.3	0.3	0.16
P3	1.13	0.41	1.9	0.16	P15	0.67	0.38	0.4	0.33
P4	0.8	0.48	0.5	0.16	P16	0.87	0.35	1.8	0
P5	0.8	0.41	1.1	0.41	P17	0.93	0.26	1.5	0.16
P6	1	0.27	2.1	0	P18	1	0.43	0.9	0
P7	1	0.30	2	0	P19	1	0.5	0.6	0.33
P8	1	0.31	1.9	0	P20	0.93	0.32	1.7	0
P9	1.07	0.23	2.4	0	P21	1.13	0.32	2.3	0
P10	1.07	0.56	2.43	0	P22	1	0.42	1.17	0.27
P11	0.93	0.32	1.3	0.16	P23	1.13	0.37	1.5	0
P12	0.67	0.50	0.8	0.16	P24	1.13	0.34	2.2	0.08

F, average of fineness number; C, classification or sorting; S, skewness; K, kurtosis.

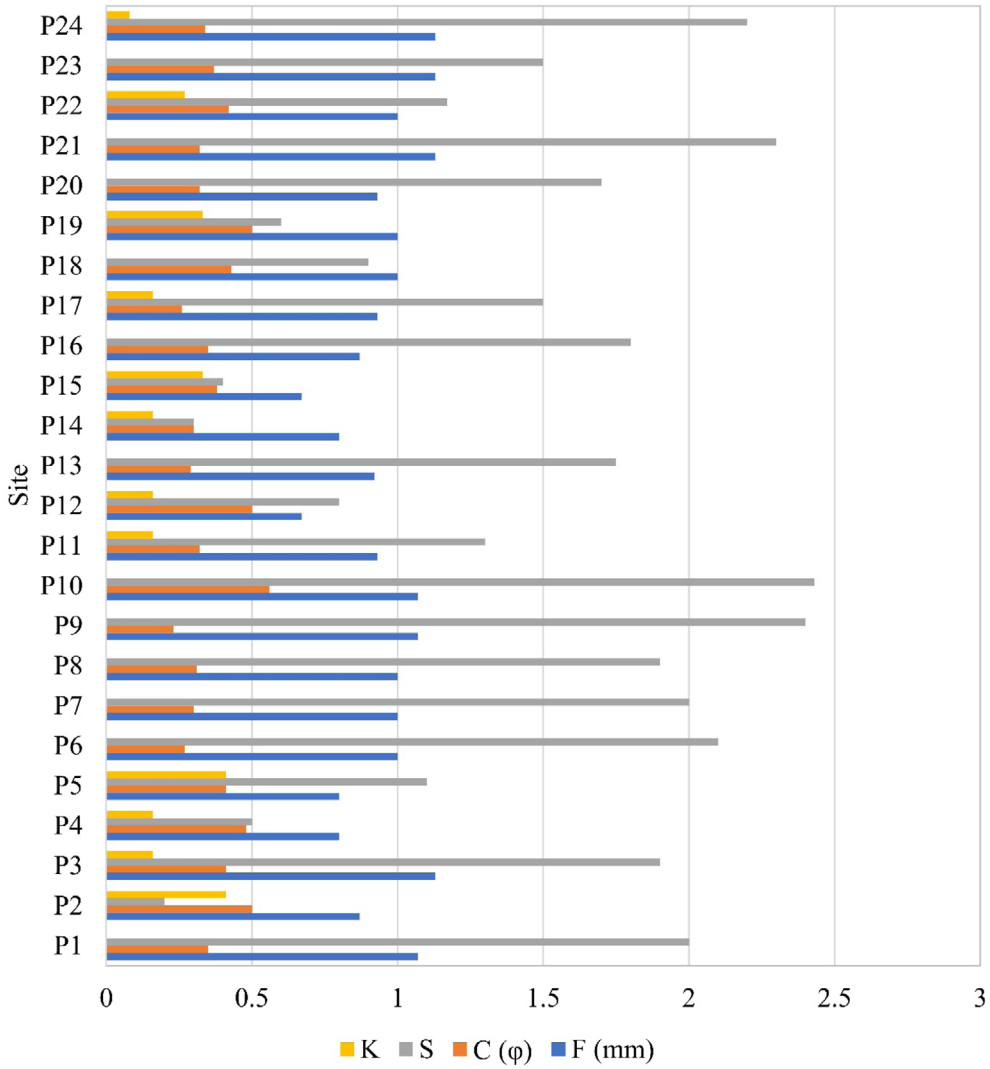

Fig. 5. Analysis of parameter by location. F represents an average of fineness number; C is classification or sorting, S is skewness, and K is kurtosis (Lee et al., 2018).

sediment consists mainly of sand. In general, values less than 0.35 φ are considered to represent very good sorting, and values up to 0.5 φ are considered good sorting. Therefore, because most sites in the Namdae-cheon stream area are in the range of

https://doi.org/10.1007/s12303-021-0011-9

0.5 φ, the sample sorting classification can be considered good. Based on the skewness test, most of the study sites showed a positive bias toward medium grain size. The kurtosis was mostly zero or positive; therefore, the distributions were generally leptokurtic. This indicates that grain size frequencies tend to accumulate in the area around the mean value or show only a small spread farther from the value of the central tendency. Sites P14, P15, and P16 on the southeast side of the estuary and sites P10, P11, P12, and P13 on the northwest side near the breach were compared. The particle size of 0.25 mm was dominant among small particles at the northwestern site, but the 1 mm particle size was dominant at the southeastern site, indicating northwestward movement of the breach.

Table 4 and Figure 6 show the average parameter for each site. The averages were calculated from sites P1–13, representing the northwest sandbar, and sites P14–P24, representing the southeast

Table 4. Analyses of parameters by depth at each site (Lee et al., 2018)

Parameter	Site Line	Depth (cm)				
		20	40	60	80	100
Average of Fineness Number	P1–P2	1	0.89	1	0.78	0.89
	P3–P5	1.08	1	1.08	1.17	1.08
	P6–P9	1	0.92	1	1	1
	P10–P13	1	1	0.92	1	0.75
	Average	1.02	0.95	1	0.99	0.93
	P14–P16	0.83	0.5	1.12	0.92	0.75
	P17–P20	0.83	1	1	1	1
	P21–P22	1.08	1.37	0.83	0.92	1.12
	P23–P24	1.33	1.22	1.22	1	1.11
	Average	1.02	1.02	1.04	0.96	1
Classification	P1–P2	0.47	0.39	0.47	0.42	0.37
	P3–P5	0.38	0.31	0.41	0.39	0.49
	P6–P9	0.3	0.33	0.35	0.23	0.26
	P10–P13	0.23	0.39	0.53	0.43	0.48
	Average	0.34	0.35	0.44	0.37	0.4
	P14–P16	0.35	0.44	0.67	0.29	0.45
	P17–P20	0.46	0.39	0.46	0.28	0.35
	P21–P22	0.33	0.82	0.39	0.67	0.84
	P23–P24	0.4	0.47	0.49	0.25	0.28
	Average	0.39	0.53	0.5	0.36	0.48
Skewness	P1–P2	1.33	0.67	1	0.5	2
	P3–P5	1.87	1.87	1.75	2.12	1.25
	P6–P9	2	1.62	1.75	2.25	1.5
	P10–P13	2.25	1.62	0.12	1.5	2.79
	Average	1.86	1.45	1.16	1.59	1.88
	P14–P16	0.75	0.37	2.16	1.25	0.37
	P17–P20	0.12	1.12	0.62	2.25	1.75
	P21–P22	2.12	4.32	-0.12	2.04	4.78
	P23–P24	2.5	1	4.21	2.17	2.33
	Average	1.37	1.7	1.72	1.92	2.31
Kurtosis	P1–P2	0.27	0.27	0.55	0.14	0.14
	P3–P5	0.41	0	0	0	0.1
	P6–P9	0	0	0	0	0
	P10–P13	0	0	0.2	0	0.2
	Average	0.17	0.07	0.19	0.03	0.11
	P14–P16	0.31	0.31	1.72	0.2	0.41
	P17–P20	0.41	0.2	0	0	0
	P21–P22	0	0.92	0.31	1.33	1.69
	P23–P24	0.14	0	0	0	0
	Average	0.21	0.36	0.51	0.38	0.52

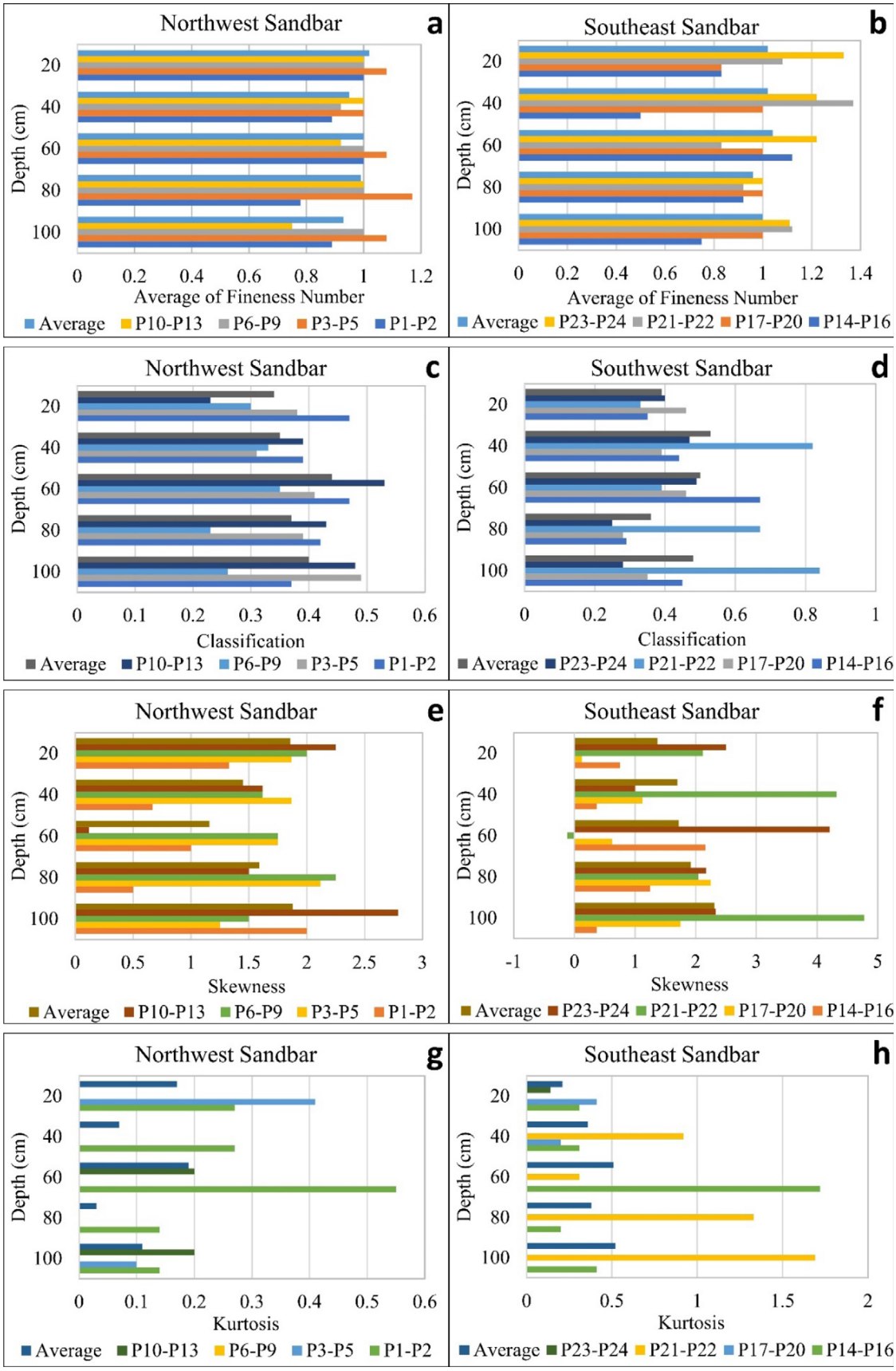

Fig. 6. Analyses of parameters by the depth at each site (northwest and southeast sandbar): (a and b) average fineness number, (c and d) classification, (e and f) skewness, (g and h) kurtosis (Lee et al., 2018).

https://doi.org/10.1007/s12303-021-0011-9

sandbar. The fineness was generally the same, around 0.9–1 mm, and particle size did not differ with depth. Most sorting classifications of samples were within 0.3–0.53 φ. The classification of the southeast sandbar site appeared to be inferior compared to that of the northwest sandbar because particles are transported from the former to the latter. In addition, skewness with depth showed a favorable leptokurtic distribution and positive kurtosis. Overall, it can be concluded that the depth of the sediment did not significantly affect grain fineness.

4. DISCUSSION

From our results, we conclude that UAV devices are useful for monitoring morphological changes caused by coastal dynamics, such as in the case of the Namdae-cheon estuary. The DSM data showed that the study area experienced significant changes in only 1 month. Figure 4 shows the morphological changes in the main stream of the study area and also the changes in sediment height of the sandbar. All results relevant for recording morphological changes can be acquired using an UAV device.

The average accuracies of the UAV images matched or were superior to previous conventional aerial images taken in both study areas. The robustness of the software (Agisoft PhotoScan) and the carefully planned GCP network seemed to be related to the positive outcomes. The target design used for GCP, whose center could easily be detected in photographs and expressed in

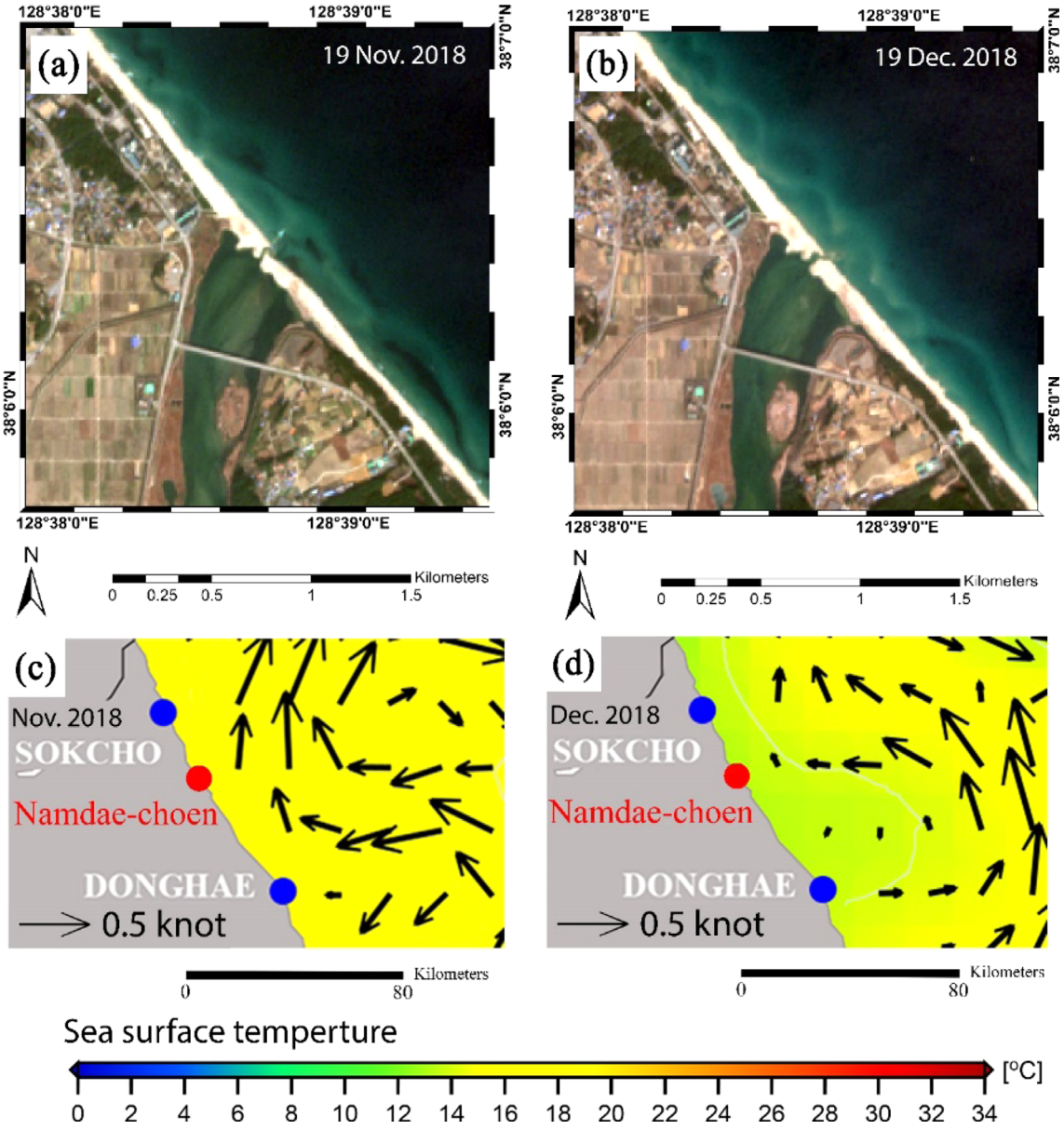

Fig. 7. Sentinel image (a and b) and monthly average surface flow and sea surface temperature (SST) data (c and d): (a and c) November 20, 2018, (c and d) December 18, 2018.

the software with a high degree of accuracy, also appears to be a primary reason. Thus, in this work, the use of appropriate GPS hardware and the existence of a network of reference stations with high accuracy allowed a high level of accuracy and data quality control.

The morphology and sedimentation of the sandbar in the Namdae-cheon estuary are influenced by several factors. We suspect two main factors: tidal action and precipitation. Savenije (2005) defined an alluvial estuary as an estuary with an erosion layer, influenced by both tidal and river flow. Thus, alluvial estuary base sediments consist of two types: fine mud and coarse fluvial sand. Depending on the relative importance of the hydrodynamic processes, one can further distinguish between river-dominated and tide-dominated estuaries. Our analyses showed that the majority of the study area has a grain size of 0.67–1.28 mm, which is within the sand size category based on the Udden-Wentworth Scale (Wentworth, 1922). Based on the grain size data, we interpreted that the study area is strongly affected by tidal factors and that the estuary is dominated by tides. Tide-dominated estuaries contain tidal sand bars at the seaward end, which are dominated by sand-sized sediment, separated from a fluvial zone, which is mostly relatively fine-grained tidal plains (Dalrymple et al., 1992).

Figure 7 shows monthly average surface flow and sea surface temperature (SST) data (Korea Hydrographic and Oceanographic Agency). We previously interpreted that the study area is dominated by tides rather than by river flow, and the monthly average surface flow and SST data are related to tides and sediment transport in the region. In November, the wind speed in the study area was 0.3–0.5 knots, and the SST was about 16–18 °C. In December, these values decreased to 0.1–0.3 knots and 13–15 °C, respectively. This indicates a decrease in energy as a medium for sediment transport, so sediment supply was decreasing, resulting in erosion on the sediment sandbar in the study area. Analyses of grain fineness, which was characterized by fining toward the northwest, showed that sediment particles move from the southeast to the northwest. This result was also supported by the monthly average flow and SST data, which showed that the movement of wind and waves was from southeast to northwest.

The second factor affecting morphological changes in the study area is precipitation. Table 5 shows precipitation data from the Sokcho area, which is the nearest rainfall observation site from the study sites. High rainfall should result in increased sediment (Rahbari Sisakht et al., 2014). The cumulative recorded rainfall before the study period was 206.5 mm, and the cumulative rainfall during the study period was 11.3 mm. The rainfall data show a drastic decline from before to after the study period. When rainfall decreases, sandbar sediments in the study area also decrease. It can be concluded that higher rainfall resulted in sediment supply prior to the study period. However, during the study period, rainfall decreased and sediment supply also decreased.

Table 5. Rainfall data in the Sokcho area

Period	Date (dd/mm/yyyy)	Precipitation (mm)
Before the research period	05/11/2018	0
	06/11/2018	9.8
	07/11/2018	152.8
	08/11/2018	27.8
	09/11/2018	0.3
	12/11/2018	0.2
	13/11/2018	10.9
	14/11/2018	4.7
	Cumulative Rainfall	206.5
During the research period	24/11/2018	0.9
	03/12/2018	2.4
	04/12/2018	7.1
	06/12/2018	0.6
	11/12/2018	0.3
	Cumulative Rainfall	11.3

Sediment deposits and reduction rates were analyzed for about 1 month from the beginning of data collection, and the results showed that about 30 cm of sediment was removed and transported to the northwest side of the mainstream. Analyses of grain fineness, sediment deposition, and erosion rate could be used to understand and predict the direction of sediment movement in the Namdae-cheon estuary. However, because it is difficult to determine trends based on the results of a single study, ongoing research and data collection are needed, and the theoretical soundness and accuracy of the approaches used in this study must be validated for them to be useful for further.

The application of UAVs for estuarine monitoring has many advantages, namely, it takes less time and requires lower costs to get data over a large area compared to the traditional field surveys. In addition, measurements can be carried out over a large area with a high spatial measurement resolution so that it can detect changes in the morphology of the dune height in the order of centimeters.

In addition to its advantages in measuring estuaries, UAV applications have several challenges from environmental conditions which can be a weakness in the application of UAV photogrammetry in coastal monitoring. These factors are changes in wind direction and speed that can affect the flying conditions of the UAV, this results in monitoring carried out using a UAV depending on weather conditions. In addition, the difficulty of maintaining artificial GCPs and automatic binding point detection is also a challenge when using UAV photos, especially for large or irregularly shaped water areas.

https://doi.org/10.1007/s12303-021-0011-9

5. CONCLUSIONS

Monitoring the Namdae-cheon estuary is very important because it is a closed estuary surrounded by a natural sandbar and thus water does not flow smoothly into the ocean and becomes stagnant. This condition is related to the very dynamic morphology of the sandbars. Our results indicate that morphological and sedimentation changes at the estuary are predominantly caused by tides but that wind speed also affects sediment accumulation and movement.

UAV devices were successfully used to monitor morphological changes caused by coastal dynamics in the estuary. This study demonstrated that UAS-based remote-sensing techniques are capable of efficiently representing and monitoring dynamic and inaccessible areas. Moreover, the combination of DSM data from UAV photos and geological data from sediment samples was useful for explaining the causative factors of morphological changes and the direction of sediment movement in the study area. The effortless operation of these devices and their ability to acquire high-resolution DSM and georeferenced imagery, along with the high temporal resolution that can be attained, can improve existing methods of mapping such areas. Nevertheless, environmental conditions such as wind speed and direction pose primary challenges for implementing UAV photogrammetry in coastal monitoring. In addition, the difficulty of retaining artificial GCPs and automatic tie-point detection are also challenges when using UAV photographs, particularly for large or irregularly shaped water areas.

ACKNOWLEDGMENTS

This work was supported by Basic Science Research Program through the National Research Foundation of Korea (NRF) funded by the Ministry of Education [No. 2019R1A6A1A03033167]. This study was supported by 2019 Research Grant (PoINT) from Kangwon National University.

REFERENCES

Archetti, R., Paci, A., Carniel, S., and Bonaldo, D., 2016, Optimal index related to the shoreline dynamics during a storm: the case of Jesolo beach. Natural Hazards and Earth System Sciences, 16, 1107–1122. https://doi.org/10.5194/nhess-16-1107-2016

Barry, P. and Coakley, R., 2013, Accuracy of UAV photogrammetry compared with network RTK GPS. International Archives of the Photogrammetry, Remote Sensing and Spatial Information Sciences, 2, 27–31.

Brasington, J., Langham, J., and Rumsby, B., 2003, Methodological sensitivity of morphometric estimates of coarse fluvial sediment transport. Geomorphology, 53, 299–316. https://doi.org/10.1016/S0169-555X(02)00320-3

Byeon, H.K., Choi, J.S., and Choi, J.K., 1996, Fish fauna and distribution characteristic of anadromous type fish in Yangyangnamdae stream. Korean Journal of Limnology, 29, 159–166.

Dalrymple, R.W., Zaitlin, B.A., and Boyd, R., 1992, Estuarine facies models; conceptual basis and stratigraphic implications. Journal of Sedimentary Research, 62, 1130–1146. https://doi.org/10.1306/D4267A69-2B26-11D7-8648000102C1865D

Deloffre, J., Lafite, R., Lesueur, P., Lesourd, S., Verney, R., and Guézennec, L., 2005, Sedimentary processes on an intertidal mudflat in the upper macrotidal Seine estuary, France. Estuarine, Coastal and Shelf Science, 64, 710–720. https://doi.org/10.1016/J.ECSS.2005.04.004

Deloffre, J., Verney, R., Lafite, R., Lesueur, P., Lesourd, S., and Cundy, A.B., 2007, Sedimentation on intertidal mudflats in the lower part of macrotidal estuaries: sedimentation rhythms and their preservation. Marine Geology, 241, 19–32. https://doi.org/10.1016/j.margeo.2007.02.011

Domeneghetti, A., 2016, On the use of SRTM and altimetry data for flood modeling in data-sparse regions. Water Resources Research, 52, 2901–2918. https://doi.org/10.1002/2015WR017967

Dyer, K.R., 1995, Sediment transport processes in estuaries. Developments in Sedimentology, 53, 423–449. https://doi.org/10.1016/S0070-4571(05)80034-2

Folk, R.L. and Ward, W.C., 1957, Brazos river bar: a study in the significance of grain size parameters. Journal of Sedimentary Research, 27, 3–26. https://doi.org/10.1306/74D70646-2B21-11D7-8648000102C1865D

Friedrichs, C., Armbrust, B.D., and De Swart, H.E., 1998, Hydrodynamics and equilibrium sediment dynamics of shallow, funnel-shaped tidal estuaries. In: Dronkers, J. and Scheffers, M. (eds.), Physics of Estuaries and Coastal Seas. Virginia Institute of Marine Science Books, Balkema, Rotterdam, 38, p. 315–327.

Green, M.O., Black, K.P., and Amos, C.L., 1997, Control of estuarine sediment dynamics by interactions between currents and waves at several scales. Marine Geology, 144, 97–116. https://doi.org/10.1016/S0025-3227(97)00065-0

Gülch, E., 2011, Photogrammetric evaluation of multi-temporal fixed wing UAV imagery. International Archives of the Photogrammetry, Remote Sensing and Spatial Information Sciences, XXXVIII-1/C22, 265–270. https://doi.org/10.5194/isprsarchives-XXXVIII-1-C22-265-2011

Gurnell, A.M., Corenblit, D., García de Jalón, D., González del Tánago, M., Grabowski, R.C., O'Hare, M.T., and Szewczyk, M., 2016, A conceptual model of vegetation-hydrogeomorphology interactions within river corridors. River Research and Applications, 32, 142–163. https://doi.org/10.1002/rra.2928

Haala, N., Cramer, M., Weimer, F., and Trittler, M., 2011, Performance test on UAV-based photogrammetric data collection. International Archives of the Photogrammetry, Remote Sensing and Spatial Information Sciences, XXXVIII-1/C22, 7–12. https://doi.org/10.5194/isprsarchives-XXXVIII-1-C22-7-2011

Haubeck, K. and Prinz, T., 2013, A UAV-based low-cost stereo camera system for archaeological surveys-experiences from doliche (Turkey). International Archives of the Photogrammetry, Remote Sensing and Spatial Information Sciences, XL-1/W2, 195–200. https://doi.org/10.5194/isprsarchives-XL-1-W2-195-2013

Jaud, M., Passot, S., Le Bivic, R., Delacourt, C., Grandjean, P., Le Dantec, N., Jaud, M., Passot, S., Le Bivic, R., Delacourt, C., Grandjean, P., and Le Dantec, N., 2016, Assessing the accuracy of high resolution digital surface models computed by photoscan® and micmac® in sub-

optimal survey conditions. Remote Sensing, 8, 465. https://doi.org/10.3390/rs8060465

Javernick, L., Brasington, J., and Caruso, B., 2014, Modeling the topography of shallow braided rivers using structure-from-motion photogrammetry. Geomorphology, 213, 166–182. https://doi.org/10.1016/J.GEOMORPH.2014.01.006

Krumbein, W.C., 1934, Size frequency distributions of sediments. Journal of Sedimentary Research, 4, 65–77. https://doi.org/10.1306/D4268EB9-2B26-11D7-8648000102C1865D

Küng, O., Strecha, C., Beyeler, A., Zufferey, J.-C., Floreano, D., Fua, P., and Gervaix, F., 2011, The accuracy of automatic photogrammetric techniques on ultra-light UAV imagery. International Archives of the Photogrammetry, Remote Sensing and Spatial Information Sciences, XXXVIII-1/C22, 125–130. https://doi.org/10.5194/isprsarchives-XXXVIII-1-C22-125-2011

Langhammer, J., Bernsteinová, J., and Miřijovský, J., 2017, Building a high-precision 2D hydrodynamic flood model using UAV photogrammetry and sensor network monitoring. Water, 9, 861. https://doi.org/10.3390/w9110861

Lee, Y.I., Choi, T., and Lim, H.S., 2016, Depositional age and petrological characteristics of the Jangsan formation in the Taebaeksan basin, Korea-revisited. Journal of the Geological Society of Korea, 52, 67–77. https://doi.org/10.14770/jgsk.2016.52.1.67

Lee, S., Park, S., and Lee, C.-W., 2018, Monitoring of moisture content and sediment fineness as predictors of shoal breaching in an estuary. Journal of the Korean Society of Surveying, Geodesy, Photogrammetry and Cartography, 36, 25–32. https://doi.org/10.7848/ksgpc.2018.36.1.25

Lucieer, A., Turner, D., King, D.H., and Robinson, S.A., 2014, Using an unmanned aerial vehicle (UAV) to capture micro-topography of antarctic moss beds. International Journal of Applied Earth Observation and Geoinformation, 27, 53–62. https://doi.org/10.1016/j.jag.2013.05.011

Marion, A., Nikora, V., Puijalon, S., Bouma, T., Koll, K., Ballio, F., Tait, S., Zaramella, M., Sukhodolov, A., O'Hare, M., Wharton, G., Aberle, J., Tregnaghi, M., Davies, P., Nepf, H., Parker, G., and Statzner, B., 2014, Aquatic interfaces: a hydrodynamic and ecological perspective. Journal of Hydraulic Research, 52, 744–758. https://doi.org/10.1080/00221686.2014.968887

Maune, D.F., 2001, Digital Elevation Model Technologies and Applications: The DEM Users Manual (1st edition). American Society for Photogrammetry and Remote Sensing(ASPRS) Publications, Bethesda, 539 p.

Moretto, J., Rigon, E., Mao, L., Picco, L., Delai, F., and Lenzi, M.A., 2014, Channel adjustments and island dynamics in the brenta river (Italy) over the last 30 years. River Research Applications, 30, 719–732. https://doi.org/10.1002/rra.2676

Nones, M. and Di Silvio, G., 2016, Modeling of river width variations based on hydrological, morphological, and biological dynamics. Journal of Hydraulic Engineering, 142, 04016012. https://doi.org/10.1061/(ASCE)HY.1943-7900.0001135

Payne, C., Panda, S., and Prakash, A., 2018, Remote sensing of river erosion on the Colville river, north slope Alaska. Remote Sensing, 10, 397. https://doi.org/10.3390/rs10030397

Rahbari Sisakht, S., Majnounian, B., Mohseni Saravi, M., Abdi, E., and Surfleet, C., 2014, Impact of rainfall intensity and cutslope material on sediment concentration from forest roads in northern Iran. iForest - Biogeosciences and Forestry, 7, 48–52. https://doi.org/10.3832/IFOR0097-007

Remondino, F., Barazzetti, L., Nex, F., Scaioni, M., and Sarazzi, D., 2011, UAV photogrammetry for mapping and 3D modeling-current status and future perspectives. International Archives of the Photogrammetry Remote Sensing and Spatial Information Sciences, XXXVIII-1/C22, 25–31. https://doi.org/10.5194/isprsarchives-XXXVIII-1-C22-25-2011

Rosnell, T. and Honkavaara, E., 2012, Point cloud generation from aerial image data acquired by a quadrocopter type micro unmanned aerial vehicle and a digital still camera. Sensors, 12, 453–480. https://doi.org/10.3390/s120100453

Savenije, H.H.G., 2012, Salinity and tides in alluvial estuaries (2nd completely revised edition). https://salinityandtides.com/ [Accessed on 25 May 2021].

Scorpio, V., Zen, S., Bertoldi, W., Surian, N., Mastronunzio, M., Dai Prá, E., Zolezzi, G., and Comiti, F., 2018, Channelization of a large Alpine river: what is left of its original morphodynamics? Earth Surface Process and Landforms, 43, 1044–1062. https://doi.org/10.1002/esp.4303

Siebert, S. and Teizer, J., 2014, Mobile 3D mapping for surveying earthwork projects using an unmanned aerial vehicle (UAV) system. Automation in Construction, 41, 1–14. https://doi.org/10.1016/J.AUTCON.2014.01.004

Spiekermann, R., Betts, H., Dymond, J., and Basher, L., 2017, Volumetric measurement of river bank erosion from sequential historical aerial photography. Geomorphology, 296, 193–208. https://doi.org/10.1016/j.geomorph.2017.08.047

Udden, J.A., 1898, The Mechanical Composition of Wind Deposits. Augustana Library Publications No. 1, Augustana College and Theological Seminary, Rock Island, 69 p.

Vallet, J., Panissod, F., Strecha, C., and Tracol, M., 2011, Photogrammetric performance of an ultra light weight swinglet "UAV". International Archives of the Photogrammetry, Remote Sensing and Spatial Information Sciences, XXXVIII-1/C22, 253–258. https://doi.org/10.5194/isprsarchives-XXXVIII-1-C22-253-2011

Wentworth, C.K., 1922, A scale of grade and class terms for clastic sediments. The Journal of Geology, 30, 377–392. https://doi.org/10.1086/622910

Wheaton, J.M., Brasington, J., Darby, S.E., and Sear, D.A., 2010, Accounting for uncertainty in DEMs from repeat topographic surveys: improved sediment budgets. Earth Surface Process and Landforms, 35, 136–156. https://doi.org/10.1002/esp.1886

Woodget, A.S., Carbonneau, P.E., Visser, F., and Maddock, I.P., 2015, Quantifying submerged fluvial topography using hyperspatial resolution UAS imagery and structure from motion photogrammetry. Earth Surface Process and Landforms, 40, 47–64. https://doi.org/10.1002/esp.3613

Yoon, Y.Y., Kim, D.H., and Lee, S.M., 1999, Accumulation of pollutants in the lower course of the namdae stream and effect of the water discharged from Kangnung hydroelectric power station. Journal of Korean Society of Environmental Engineers, 21, 2221–2230.